

# Characterizing the Galactic warp with Gaia: I. The tilted ring model with a twist

Hoda Abedi<sup>1\*</sup>, Cecilia Mateu<sup>2,3</sup>, Luis A. Aguilar<sup>2</sup>, Francesca Figueras<sup>1</sup>  
and Mercè Romero-Gómez<sup>1</sup>

<sup>1</sup> *Dept. d'Astronomia i Meteorologia, Institut de Ciències del Cosmos, Universitat de Barcelona, IEEC, Martí i Franquès 1, E08028 Barcelona, Spain*

<sup>2</sup> *Instituto de Astronomía, UNAM, Apartado Postal 877, 22860 Ensenada, B.C., Mexico*

<sup>3</sup> *Centro de Investigaciones de Astronomía, AP 264, Mérida 5101-A, Venezuela*

Accepted. Received ; in original form

## ABSTRACT

We explore the possibility of detecting and characterizing the warp of the stellar disc of our Galaxy using synthetic Gaia data. The availability of proper motions and, for the brightest stars radial velocities, adds a new dimension to this study. A family of Great Circle Cell Counts (GC3) methods is used. They are ideally suited to find the tilt and twist of a collection of rings, which allow us to detect and measure the warp parameters. To test them, we use random realizations of test particles which evolve in a realistic Galactic potential warped adiabatically to various final configurations. In some cases a twist is introduced additionally. The Gaia selection function, its errors model and a realistic 3D extinction map are applied to mimic three tracer populations: OB, A and Red Clump stars. We show how the use of kinematics improves the accuracy in the recovery of the warp parameters. The OB stars are demonstrated to be the best tracers determining the tilt angle with accuracy better than  $\sim 0.5$  up to Galactocentric distance of  $\sim 16$  kpc. Using data with good astrometric quality, the same accuracy is obtained for A type stars up to  $\sim 13$  kpc and for Red Clump up to the expected stellar cut-off. Using OB stars the twist angle is recovered to within  $< 3^\circ$  for all distances.

**Key words:** Galaxy: structure, Galaxy: kinematics and dynamics, Galaxy: disc, methods: numerical

## 1 INTRODUCTION

It is widely accepted that warps of disc galaxies are a common phenomena (as common as spiral structure), yet they are still not fully understood (see García-Ruiz et al. (2002) for a historical review). From observational studies in external galaxies, Briggs's laws (Briggs 1990) state that discs are generally flat inside the  $R_{25}$  radius that is inside the solar Galactocentric radius in our Milky Way (MW); the line of nodes is straight out to  $R_{26.5}$ , indicating that the self-gravity of the disc is important; and, farther out the line of nodes advances in the direction of galactic rotation indicating that the warps are not quite in equilibrium at large radii. Note that  $R_{25}$  and  $R_{26.5}$  are the radius of galaxy to the respectively 25 mag arcsec<sup>-2</sup> and 26.5 mag arcsec<sup>-2</sup> isophotes. As discussed by Cox et al. (1996), as the stellar warps usually follow the same warped surface as do the gaseous ones, there is strong evidence that warps are mainly a gravitational

phenomenon. Furthermore, as Sellwood (2013) stated, the ubiquity of warps in external galaxies suggests that they are either, repeatedly regenerated, or a long-lived phenomenon. In any case, warped discs represent a theoretical challenge and, if properly understood, can be a valuable probe into the mass distribution in the outer disc and the halo in its vicinity (Binney 1992).

From the time when the first 21-cm observations of our Galaxy became available, the large-scale warp in the HI gas disc became apparent (Burke 1957; Westerhout 1957; Oort et al. 1958, among others). More than fifty years later, Levine et al. (2006) has re-examined the outer HI distribution proposing that the warp of gas is well described by two Fourier modes, the  $m=2$  mode accounting for a large asymmetry between the northern ( $l = 90^\circ$ ) and southern warps ( $l = 270^\circ$ ). Meanwhile, Reylé et al. (2009), from the dust and stars distribution, using 2MASS infrared data, found the stellar component, in a first approximation, to be well modelled by an S-shaped warp with a significantly smaller slope than the one seen in the HI warp. Several authors

\* e-mail: habedi@am.ub.es

have tried to estimate the phase angle of the line of nodes with respect to the Sun-Galactic centre line. Values range between  $\sim -5^\circ$  (López-Corredoira et al. 2002) and  $\sim 15^\circ$  (Momany et al. 2006). These morphological studies of the MW warp do not allow us, at present, to disentangle which are the mechanisms that are able to explain it.

Many efforts have been directed toward understanding warps on a theoretical basis and, at least, three mechanisms have been proposed for their existence (see the excellent reviews by Binney et al. 1998; Sellwood 2013). One of these mechanisms posits that warps are free normal modes of oscillation of the galactic disc. Lynden-Bell (1965) suggested that warps could result from a persisting misalignment between the spin axis and the disc normal, a suggestion that was later elaborated by Hunter & Toomre (1969). From these pioneer works, the bending modes have long been suspected as the mechanism creating and maintaining warps. The distribution of matter in the halo would control the ability of the disc to sustain a long-lived bending wave. In this context, Sparke & Casertano (1988) proposed that an axisymmetric, but flattened halo, could not wind up into corrugation waves but continue, indefinitely as a standing wave in the disc. However, it was found that a careful arrangement in the mass distribution (shape and density profile) is needed to obtain these long-lived modes, making this an unlikely scenario. On top of this, it turns out that the response of the halo to the warped disc distribution, which was not taken into account in the original mode calculations, invalidates this approach. Binney et al. (1998) stated that none of these mechanisms is viable, the only surviving explanation is that the warps are driven by the accretion of material (also discussed in López-Corredoira et al. 2002; Olano 2004), that is, by the accretion of angular momentum. The tidal interaction between galaxies (forcing by satellites) has also been proposed to produce asymmetrical warps. As an example, Levine et al. (2006) and Weinberg & Blitz (2006) proposed that a passage of the Large Magellanic Cloud could have generated the Galactic warp. Nowadays it seems that these satellite tides are generally too weak to produce warps of the amplitude observed.

The first kinematic warp analysis was inferred from Hipparcos proper motions of OB type stars (Drimmel et al. 2000). These authors concluded that the kinematics observed toward the anticentre were inconsistent with the ones expected for a long-lived warp, showing that only a very high bias in the photometric distances and/or a high warp precession rate could explain the observations. Later, Bobylev (2010), using the Tycho-2 kinematic data of Red Clump (RC) stars, associated the observed rotation of the stellar system around the Sun-Galactic centre axis to the Galactic warp. However, the derived angular velocity obtained is opposite to the values previously obtained by Miyamoto & Zhu (1998). More recently, Bobylev (2013) found that the available stellar proper motion samples alone do not allow complete information to be obtained. Nevertheless, he undertook a first analysis using six-dimensional phase-space data for a small Cepheids sample. Discrepant results obtained from all these works demonstrate the difficulty, at present, to disentangle the kinematic signature of the warp from other nearby and local perturbations.

At present, what is needed is better information that could help us to disentangle among the various competing

scenarios. The warp of our own Galaxy is the one closest to us and thus, potentially a lot of detailed information may be gleaned from it. At the dawn of the Gaia era, a whole hitherto unexplored dimension opens up: adding good kinematical information of in situ stars partaking in the warp. This dimension must be explored: To what extent is it that Gaia data will be able to characterize the stellar disc warp and up to what distance? To answer this question, new detection and characterization tools must be devised and tested with Gaia mock catalogues and their limits identified.

In this paper we do not develop a fully self-consistent simulation of a warp, but rather a first simplified kinematic model for our MW warp. This is because it is not our goal to dwell into dynamical scenarios, but rather have a reasonable toy model with which to assess the real possibilities of Gaia in detecting and characterizing the warp. In section 2 we present the warp models used. In section 3 we describe the generation of initial conditions, the selected tracer populations and the simulation of observational errors, extinction and the Gaia selection function. In section 4 we present the family of GC3 methods and the method used to compute the warp twist and tilt angles. In section 5 we discuss our results for the different GC3 methods, tracer populations and warp models. Our conclusions and expectations for the future, when the real Gaia database becomes available are presented in section 6.

## 2 THE WARP MODEL

We model the axisymmetric part of the MW's potential following Allen & Santillan (A&S) (Allen & Santillan 1991). This 3D potential model consists of a spherical bulge, a Miyamoto-Nagai disc (Miyamoto & Nagai 1975) and a massive spherical halo. The rotation curve of this potential model follows the one of MW. The adopted observational constraints of the model are summarized in table 1 of Allen & Santillan (1991). The total axisymmetric mass is  $M_T = 9 \times 10^{11} M_\odot$ . This is in a good agreement with the recent observational value which is  $M_T = 10^{+3}_{-2} \times 10^{11} M_\odot$  (Xue et al. 2008).

A first element required to model a galactic disc warp is a transformation that can be applied to an initially flat potential function or particle configuration, and distort it according to a specific warp model. In this section we introduce two non-lopsided warp models: the untwisted warp model in which the warp is applied directly to the disk potential; and the twisted warp model, where we twist the phase-space coordinates of our particles. In this paper, the line of nodes is defined to coincide with the X-axis, which goes along the Sun-Galactic centre direction; the Y-axis perpendicular to it, positive in counter-clockwise direction as seen from the North Galactic Pole; and the Z-axis perpendicular to the flat Galactic plane.

### 2.1 The untwisted warp model

As a first warp model, we consider a non-precessing warp with a straight line of nodes, i.e. with null twist angle. To accomplish this, we rotate the Cartesian coordinates around

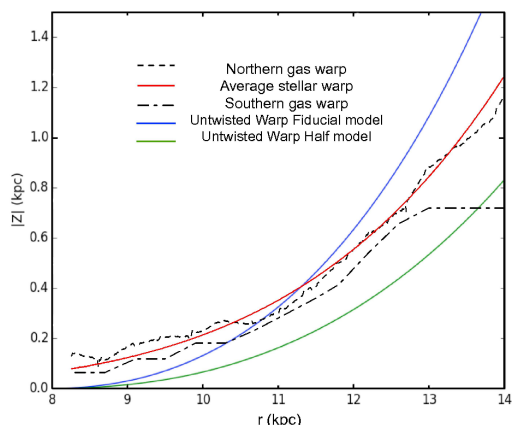


**Figure 1.** Maximum amplitude of the vertical height of the warp as a function of the Galactocentric radius for the full and half warp models respectively in blue and green. Black dashed and dot-dashed lines and the solid red line show results from observations as indicated in the legend (López-Corredoira et al. 2002).

the X-axis with tilt angle  $\psi$  that is a function of the Galactocentric spherical  $r$  coordinate of each point:

$$\psi(r; r_1, r_2, \psi_2, \alpha) = \begin{cases} 0, & r \leq r_1 \\ \psi_2 \left( \frac{r-r_1}{r_2-r_1} \right)^\alpha, & r > r_1 \end{cases} \quad (1)$$

Where  $r_1$  and  $r_2$  are the Galactocentric radii where the warp begins and finishes respectively, which are chosen to be at  $r_1 = 8$  kpc and  $r_2 = 20$  kpc. The resulting warp has a tilt angle increasing as a power law, whose exponent is  $\alpha$  and such that at  $r_2$  it has a value equal to  $\psi_2$ . From observations we know that at a Galactocentric distance of 12 kpc, the maximum height of the warp is about 630 pc (López-Corredoira et al. 2002), which corresponds to a maximum tilt angle of  $\sim 3^\circ$  at 12 kpc. By fitting our warp model to these values, we obtain:  $\alpha = 2$  and  $\psi_2 = 27^\circ$ . This model is hereafter called the Untwisted Warp Fiducial model (UWF). In Figure 1, the maximum amplitude of the warp with respect to Galactocentric radius is plotted. Our UWF model is overestimating the values obtained from the observations at large radii. So we introduce another warp model of the same properties but with  $\psi_2 = 13.5^\circ$  which we will call hereafter as the Untwisted Warp Half model (UWH). These two different warps will model two extremes of the MW’s actual warp. In what follows will use these untwisted models to warp the potential.

## 2.2 The twisted warp model

In order to model more complex shapes for the Galactic warp, we introduce a warp model with a twisted line of nodes. In this model we take the test particles that are integrated and relaxed in the warped potential modelled with the UWF and rotate their phase-space coordinates with respect to the Z-axis. Note that, this twist model is used to twist the phase-space coordinates of the particles. Here we do not apply this model to the potential, because, if we twist the line of nodes of our already warped potential, we do not expect the particles to be able to follow the potential and

reach statistical equilibrium with it. The rotation is done using the following twist angle:

$$\phi(r; r_1, r_2, \phi_{max}) = \begin{cases} 0, & r \leq r_1 \\ \phi_{max} \left( \frac{r-r_1}{r_2-r_1} \right)^2, & r > r_1 \end{cases} \quad (2)$$

As for the tilt, the twist begins at  $r_1 = 8$  kpc and finishes at  $r_2 = 20$  kpc. We consider two twist models in this paper; one with  $\phi_{max} = 20^\circ$  and other with  $\phi_{max} = 60^\circ$  which hereafter will be respectively called as TW1 and TW2 models. These values for  $\phi_{max}$  are chosen to test Gaia capabilities to measure the twist. No observational constraints for this parameter for MW’s gas or the stellar component is available at present. From external galaxies we know (according to Briggs 1990, third rule) that at large radii the line of nodes measured in the plane of the inner galaxy advances significantly in the direction of galaxy rotation for successively larger radii, so the line of nodes forms a loosely wrapped leading spiral.

## 3 BUILDING THE WARPED SAMPLES

### 3.1 The Initial conditions

We generated sets of initial conditions that follow the density distribution of a Miyamoto-Nagai disc using the parameters of the Allen & Santillan Galactic model. This is done using the Hernquist method (Hernquist 1993). The velocity field is approximated using the first order moments of the collision-less Boltzmann equation simplified with the epicyclic approximation. The asymmetric drift is taken into account in the computation of the tangential components of the velocities. We generated test particles for three different stellar populations: RC K-giant stars, and main sequence A and OB type stars. For this, we assign the corresponding scale height and velocity dispersions at the Sun’s position to each test particle sample (see Table 1). The total number of stars for each tracer are shown in Table 2. These are calculated in such a way that the number of stars of each tracer in a cylinder of radius 100 pc centred on the Sun position is normalized to the number found in this cylinder using the new Besançon Galaxy Model (Czekaj et al. 2014). We locate the Sun at Galactocentric cartesian coordinates  $(-8.5, 0, 0)$  kpc. We adopt a circular velocity for the Local Standard of Rest (LSR) of  $V_c(R_\odot) = 220 \text{ km s}^{-1}$  which is consistent with both; our imposed potential model, i.e. A&S model, and the observational constraints (McMillan & Binney 2010). Also, we consider a peculiar velocity of the Sun with respect to the LSR of  $(U, V, W)_\odot = (11.1, 12.24, 7.25) \text{ km s}^{-1}$  (Schönrich et al. 2010).

The Galactic warp is a feature of the outer parts of the Galactic disc. In order to avoid integrating the path of particles that will not be of use later, after generating the initial conditions, we discard the ones whose apocentre radius is smaller than 8 kpc. This is done using the Lindblad diagram as explained by Aguilar (2008). In Table 2 the total number of stars satisfying this condition is presented.

**Table 1.** The velocity dispersions of different stellar tracers at the Solar neighbourhood and the corresponding disc scale heights (Aumer & Binney 2009).

Tracer	RC	A	OB
$\sigma_U$ [km/s]	30	15	10
$\sigma_W$ [km/s]	16	9	6
$z_d$ [pc]	300	100	50

**Table 2.** The surface number density ( $\Sigma$ ) and the total number of stars of each tracer. Number of stars outside the lindblad hole refers to the number of stars with apocentre radius larger than 8 kpc.

Tracer	RC	A	OB
$\Sigma$ [stars/pc <sup>2</sup> ]	0.056	0.048	0.003
Number of stars	$57 \times 10^6$	$48 \times 10^6$	$3.2 \times 10^6$
Number of stars outside the Lindblad hole	$36 \times 10^6$	$30 \times 10^6$	$1.8 \times 10^6$

### 3.2 Relaxation and steady state

We apply our untwisted warp models to the Miyamoto-Nagai disc potential of A&S. In order to be able to integrate the test particles in this warped potential, we calculate the corresponding warped forces (See Appendix A for details). Starting from a set of test particles that are relaxed in the A&S potential, if we abruptly bend the disc potential, the particles will loose their near-circular orbits and increase their velocity dispersion. To avoid this, we should warp the potential adiabatically, in other words, we should do it slowly enough, so that the particles can follow the bended potential and not be left behind. To do this, we make  $\psi_2$  a function that grows with time and reaches its maximum value  $\psi_{max}$  at time  $t_{grow}$ . To describe a gradual increase, we use the following function from Dehnen (2000):

$$\psi_2 = \psi_{max} \left( \frac{3}{16} \xi^5 - \frac{5}{8} \xi^3 + \frac{15}{16} \xi + \frac{1}{2} \right), \quad \xi \equiv 2 \frac{t}{t_{grow}} - 1. \quad (3)$$

Where  $-1 \leq \xi \leq 1$  and  $\psi_2$  varies smoothly and has null derivatives at both ends of the range. In order to get an idea of how slow the warping process should be, we run some test simulations with one particle at an initial circular orbit at 14 kpc from the Galactic centre. In Figure 3 we plot the integrated path of this particle while the potential is gradually being warped. The warping is introduced progressively through a time  $t_{grow} = n \times P$  where  $P$  is the orbital period of a star with a circular orbit at 20 kpc in the A&S potential. In the quickly warped potential, the particle acquires a sizeable amount of motion orthogonal to the instantaneous plane of the warped disc potential, whereas in the adiabatic case, the particle moves along this warped disc. In order to warp the potential in the adiabatic regime we choose  $t_{grow} = 6P$  which is about 3.5 Gyr<sup>1</sup>.

<sup>1</sup> This is not meant to be an actual time-scale in which a warping may develop in a real galactic disc, as we are not simulating an actual warping mechanism. Rather, this is the time-scale for our warping transformation meant to provide us with a reasonable set of particles within a warped potential

We use a 7-8 th order Runge-Kutta integrator with adaptive time step (Dormand & Prince 1981). The integration is done in three stages. First the test particles get relaxed in the A&S potential, the integration time at this stage depends on the velocity dispersion of the tracer, the colder they are, the more time they need to reach the statistical equilibrium with the potential. We integrate RC stars for 10 Gyr, A type stars for 20 Gyr and OB stars for 30 Gyr. Next, we adiabatically warp the potential for  $t_{grow} = 3.5$  Gyr. In the last part, we integrate the particles in the final state of the warped potential for  $t_2 = 2P$  to let the particles relax in this newly warped potential<sup>2</sup>. During the stages where the potential is time independent, energy conservation was better than 0.01% in all cases. For the cases where we want to generate a twisted warp, twisting the line of nodes (see Sec. 2.2) is done at this point, i.e. after finishing the integration. The samples we get here are the *Perfect samples* to which we will refer later in this paper.

A point that must be considered is that, when applying a geometrical transformation to a potential, the corresponding density (in the sense of being proportional to the Laplacian of the transformed potential) does not coincide with the density that is obtained from applying the transformation to the original density function. This may introduce a discrepancy, in the sense that the parameters of the estimated warp (obtained using the test particle distribution) do not coincide with those that were applied to the potential. However, we must point out that we are only recovering the tilt and twist angles that define the transformed planes of symmetry of the original functions and these do coincide, as the Laplacian preserves these planes. This is shown in figure 2, where we present the equipotentials of the warped Miyamoto-Nagai disc potential (UWF model), together with the isodensity contours of the corresponding density function.

### 3.3 The Gaia “observed samples”

#### 3.3.1 The Gaia selection function

We want to study how Gaia can improve our knowledge of the warp. Then it is necessary to determine which ones of our simulated stars can be observed by Gaia.

Measuring the unfiltered (white) light in the range of 350–1000 nm, Gaia yields  $G$  magnitudes. Stars brighter than  $G = 20$  can be observed. The Radial Velocity Spectrometer (RVS) implemented inside Gaia, provides radial velocities through Doppler-shift measurements. This instrument will integrate the flux of the spectrum in the range of 847–874 nm (region of the CaII triplet) which can be seen as measured with a photometric narrow band yielding  $G_{RVS}$  magnitudes. These measurements are collected for all stars up to  $G_{RVS} = 17$ .

For the sample whose kinematics mimics RC stars, we assign an absolute magnitude of  $M_k = -1.61$  (Alves 2000) and an intrinsic colours of  $(J - K)_o = 0.55$  (Straižys & Lazauskaitė 2009),  $(V - I)_o = 1.0$  and  $(V -$

<sup>2</sup> Again, we do not pretend this is an actual time during which real stars have orbited unperturbed around the Galaxy. This is just a time to relax our initial conditions within the assumed potential.



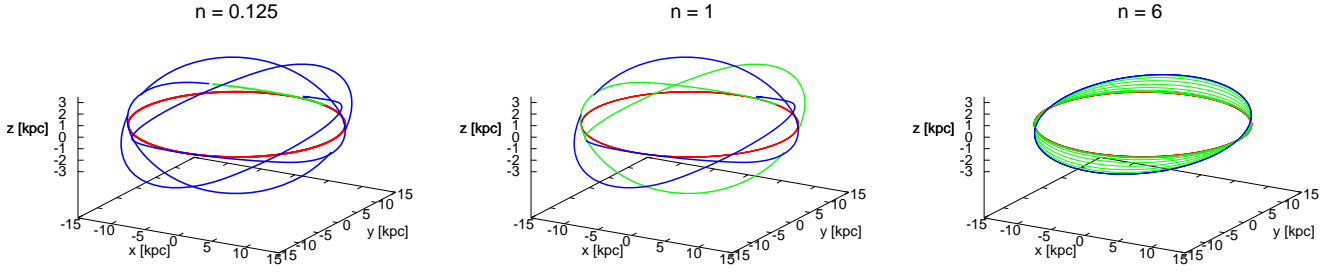


**Figure 3.** The orbit of a star with an initial circular orbit with a Galactocentric radius of 14 kpc integrated for  $t_1 = 2P$  in the A&S potential with a flat Miyamoto-Nagai disc (in red), then integrated for  $t_{grow} = n \times P$  while the disc potential is gradually being warped as a function of time (see Equation 3) (in green) and finally integrated for  $t_2 = 2P$  in the final state of the warped potential (in blue). Each panel shows the orbits for different values of  $n$ . Note that  $P$  is the orbital period of a star with a circular orbit in the A&S potential located at 20 kpc. It is clear that as we increase the value of  $n$ , i.e. warping the potential slower, the star can follow the potential more closely and acquire less motion orthogonal to the instantaneous plane of the warped disc potential. Choosing  $n = 6$ , the potential is being warped adiabatically enough that the star can keep its circular orbit within the warped plane.

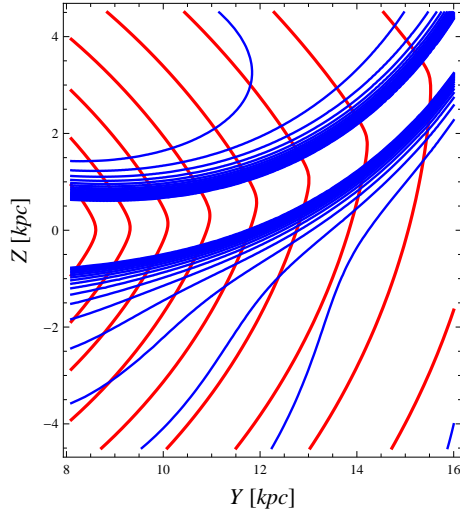


**Figure 2.** The equipotential and isodensity contours of the warped Miyamoto-Nagai disc potential of the A&S model respectively in red and blue. The plot is done in the Y-Z plane for  $X=0$ . It is clear that the position of the warped plane coincides for both, warped potential and warped density function.

$K)_o = 2.34$  (Alves 2000) to each star. We calculate the visual absorption using the 3D extinction map of Drimmel et al. (2003) using rescaling factors. The rescaling factors are used to correct the dust column density of the smooth model to account for small scale structure not described explicitly in the parametric dust distribution model. Using the extinction laws from Cardelli, Clayton & Mathis (1989), we calculate the apparent K magnitude and observed colour for every individual star. The G magnitude is then calculated as a function of K apparent magnitude and  $(J - K)$  observed colour as follows (J.M. Carrasco, private communication):

$$G = K - 0.286 + 4.023(J - K) - 0.35(J - K)^2 + 0.021(J - K)^3 \quad (4)$$

$$G_{RVS} = K - 0.299 + 2.257(J - K) + 0.042(J - K)^2 - 0.002(J - K)^3 \quad (5)$$

For A stars, the visual absolute magnitudes are assigned using the luminosity function from Murray et al. (1997) to generate stars in the range of  $[A0, A9]$ . The  $(V - I_C)$  colours are obtained from the absolute magnitude and colour relation presented in Kenyon & Hartmann (1995). For OB stars, the visual absolute magnitudes are obtained using the luminosity function from Mottram et al. (2011). The corresponding  $(V - I_C)$  colours are calculated using the absolute magnitude, effective temperature and colour relations presented in Mottram et al. (2011) and Jordi et al. (2010). The G and  $G_{RVS}$  magnitudes for the two latter mentioned tracers are calculated using the third order polynomial fit of  $V$  apparent magnitudes and  $(V - I_C)$  observed colours of Jordi et al. (2010). Considering stars with  $G < 20$ , in Figure 4 we plot the surface density of stars in X-Y and Y-Z cartesian projections for the three tracers. Looking at the Y-Z projection, the warped shape of the disc is clearly seen even after applying the Gaia selection function. From the X-Y projections it is clear that A stars are less visible to Gaia in the first and fourth quadrants compared to RC and OB stars since they are not as bright as OB stars, or as red as RC stars. As expected, the RC population has a larger scale height as seen in Y-Z projection.

### 3.3.2 The Gaia error model

The Gaia web-page<sup>3</sup> provides science performance estimates and models for errors in astrometric, photometric and spectroscopic data. The end-of-mission parallax errors depend on G magnitudes and  $(V - I_C)$  colours. Figure 5 shows the mean parallax accuracy horizons for stars with different spectral types that represent our three tracers. We also take into account the variation of errors as a function of ecliptic coordinates, due to the variation of number of transits at the end of the mission. The Galactic coordinates and proper motion

<sup>3</sup> <http://www.cosmos.esa.int/web/gaia/science-performance>

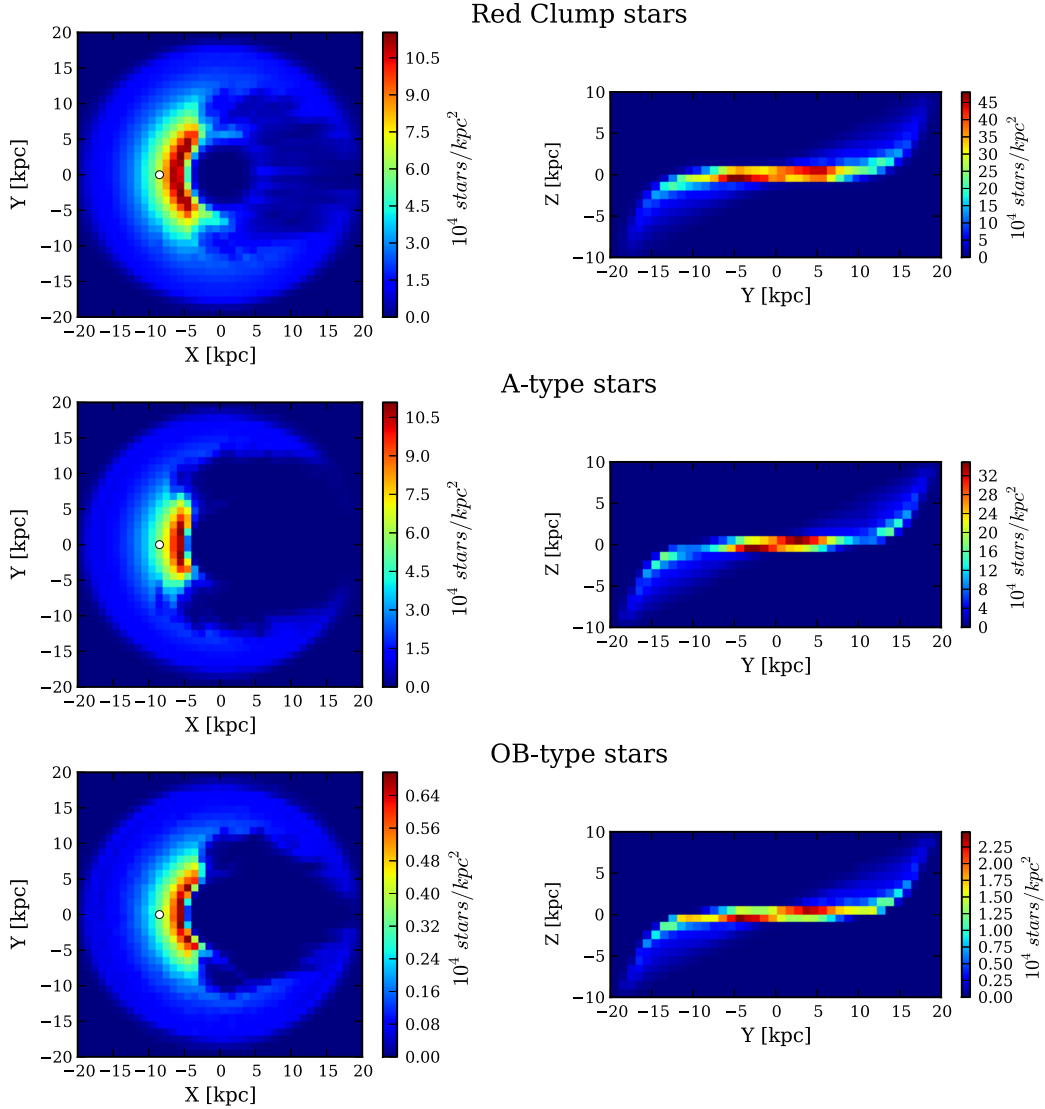


**Figure 4.** The distribution of stars of each warped tracers (warped with UWF model) in X-Y (left panels) and Y-Z (right panels) planes. These are the stars observable with Gaia ( i.e. with apparent magnitudes  $G < 20$ ). The distribution of RC, A and OB stars are shown in the top, middle and bottom panels respectively. The colour scale indicates the surface density ( $10^4 \text{ stars/kpc}^2$ ). This scale is different for each tracer population to better illustrate the surface density. The 3D extinction map of Drimmel et al. (2003) is used for calculating the apparent magnitudes. Note that the Sun is located at  $(x, y, z) = (-8.5, 0, 0)$  kpc as labelled with a white filled circle in the left panels. Therefore, in the Y-Z projection, the Sun is projected on top of the Galactic centre at  $Y=0$ . It is worth mentioning that the distances used in this plot are true distances.

errors are described as a function of the error in parallax. The end-of-mission radial velocity errors depend on  $V$  magnitudes and the spectral type of the stars. The redder they are, the smaller error in their radial velocity measurements. Applying the 3D extinction map, Gaia observational constraints and these error models to our perfect sample, we generate the Gaia “observed catalogues” for the three tracers.

### 3.3.3 Characteristics of the observed samples with and without velocity information

It is essential for our study to know how many stars will be observed by Gaia as a function of Galactocentric radius for each tracer population. We also have to know for how many of them Gaia provides radial velocity information and also how many with good parallax measurements. Figure 6 shows the histograms in logarithmic scale of the number of stars

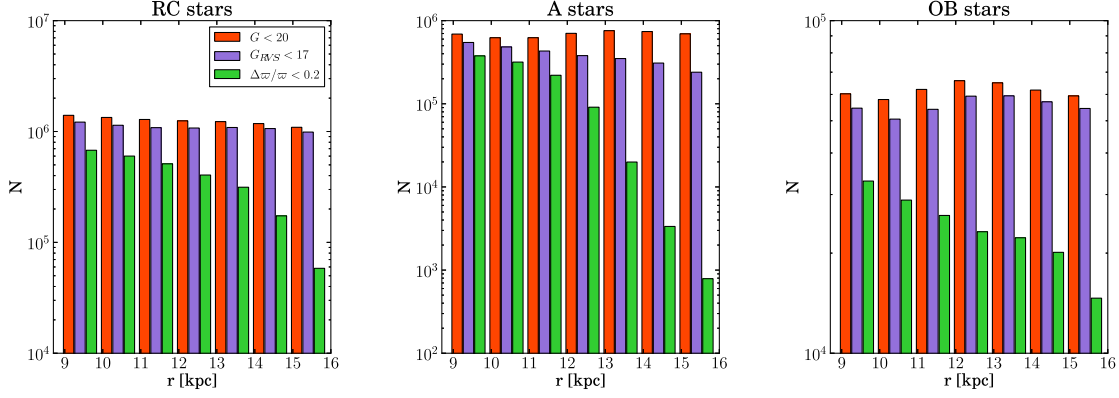


**Figure 6.** Histograms of the number of stars in Galactocentric radius bins of 1 kpc. The samples with  $G < 20$ ,  $G_{RVS} < 17$  and  $\Delta\pi/\pi < 0.2$  are shown respectively in red, purple and green. The histograms are plotted for RC stars (left panel), A stars (middle) and OB stars (right).

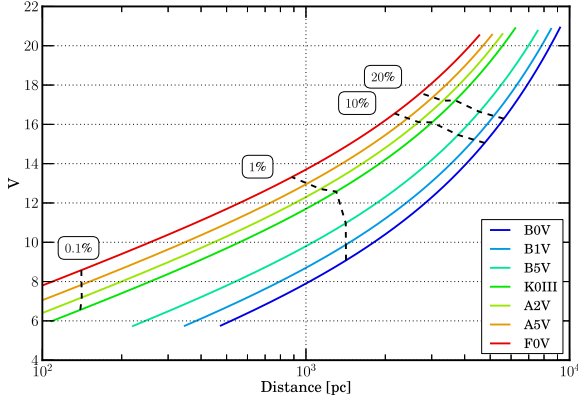


**Figure 5.** The mean parallax accuracy horizons for stars of different spectral type that represent our three tracer populations. The plot of visual apparent magnitude versus heliocentric distance is done assuming an extinction of 1 magnitude per 1 kpc. Dashed lines represent the constant line of mean relative parallax accuracy. Note that the lines of fixed relative error for stars brighter than  $V \sim 12$  are almost vertical due to the Gaia observing strategy (gates are introduced to avoid saturation).

in (spherical) Galactocentric radius bins of 1 kpc, starting from 9 kpc up to 16 kpc for the three tracers. It is worth noting that for the samples with error in parallax less than 20% ( $\Delta\pi/\pi < 0.2$ ) the number of A stars drops down by three orders of magnitude at large radii while this reduction is only one order of magnitude and less than one for RC and OB stars respectively.

## 4 WARP DETECTION AND CHARACTERIZATION

### 4.1 The mGC3 method

The modified Great Circle Cell Counts method (mGC3) was introduced by Mateu et al. (2011) as a technique for the detection of tidal streams in the Galactic

Halo, based on the original GC3 method proposed by Johnston, Hernquist & Bolte (1996) for the same purpose. The mGC3 method is based on the fact that, in a spherical potential, the tidal stream produced by the disruption of a satellite in the Galactic Halo will conserve its total angular momentum and its orbit will be confined to a plane, which will be an exactly constant plane if the potential is perfectly spherical, or will precess if it is axisymmetric. Therefore, as seen from the Galactic centre, the stars in the stream are confined to a great circle band, the projection of the orbital plane. This means that *both* the Galactocentric position and velocity vectors of stream stars are perpendicular, within a certain tolerance, to the normal vector or *pole*  $\hat{\mathbf{L}}$  which defines this particular great circle.

The mGC3 method thus consist in producing a *pole count map*<sup>4</sup>, i.e. a map of the number of stars associated to each possible pole (and therefore great circle cell) in a grid in spherical coordinate angles (directions), computed as the number of stars which, for each pole, fulfil the following criteria

$$|\hat{\mathbf{L}}_i \cdot \hat{\mathbf{r}}_{\text{gal}}| \leq \delta_r \quad \text{and} \quad |\hat{\mathbf{L}}_i \cdot \hat{\mathbf{v}}_{\text{gal}}| \leq \delta_v \quad (6)$$

where  $\hat{\mathbf{r}}_{\text{gal}}$  and  $\hat{\mathbf{v}}_{\text{gal}}$  are unit vectors in the direction of the star's (Galactocentric) position and velocity vectors respectively,  $\delta_r$  and  $\delta_v$  are the tolerances and  $\hat{\mathbf{L}}_i$  is the  $i$ -th vector on the grid of all poles considered. The modification mGC3 introduces to the original GC3 method is the use of the velocity criterion in Equation 6, which as shown in Mateu et al. (2011), increases the efficiency of the method by reducing substantially the background contamination. Also, in order to avoid the distance bias introduced by the reciprocal of the parallax (Brown et al. 2005), Mateu et al. (2011) use the criteria of Equation 6 expressed in the following equivalent manner

$$|\hat{\mathbf{L}}_i \cdot \mathbf{r}'_{\text{gal}}| \leq \|\mathbf{r}'_{\text{gal}}\| \delta_r \quad \text{and} \quad |\hat{\mathbf{L}}_i \cdot \mathbf{v}'_{\text{gal}}| \leq \|\mathbf{v}'_{\text{gal}}\| \delta_v \quad (7)$$

<sup>4</sup> The Python package PyMGC3 containing code to run the mGC3/nGC3/GC3 family of methods is publicly available at the github repository <https://github.com/cmteu/PyMGC3>

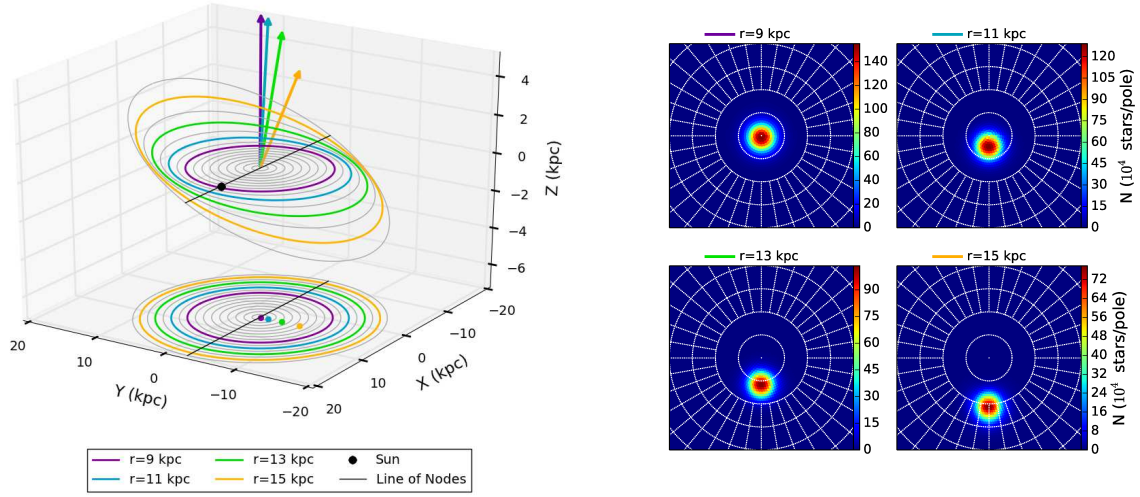


**Figure 7.** *Left:* Schematic plot of a warped disc (UWF model). The solid black line and black dot indicate respectively the line of nodes and the Sun's position. Concentric circles shown in gray increase in Galactocentric radius by 1 kpc, with colours showing four selected rings at 9 (purple), 11 (blue), 13 (green) and 15 kpc (orange). The arrows represent the normal vectors corresponding to each of these rings, in the same colour. The projection in the X-Y plane shows the tips of the normal vectors, aligned along the direction perpendicular to the line of nodes, which in this case is a straight line. *Right:* The  $2 \times 2$  mosaic shows the pole count maps which correspond to stars in spherical shells with the same radii as the coloured rings indicated in the left panel. The simulated A stars are used to generate these plots. The maps are shown in an a north-polar azimuthal equidistant projection, showing the north pole at the centre,  $\varphi = 90^\circ - 270^\circ$  in the vertical direction at the centre of the plot, the concentric circles have a separation of  $5^\circ$ , and meridians are drawn at  $10^\circ$  intervals in longitude. The colour scale shows the number of stars associated to each pole according to the mGC3 criteria of Equation 7. Each of the pole vectors indicated by the arrows in the left panel correspond to the pole with maximum counts in the pole count map for the respective radius. The sequence of plots clearly shows how the position of the pole with the maximum star counts shifts in latitude as the radius  $r$  increases, as do the arrows shown in the left panel, as a consequence of the increase in the tilt angle  $\psi(r)$ . The azimuthal angle  $\varphi$  of the maximum counts pole (and the corresponding arrows) remains constant as expected for a straight line of nodes.

where  $\mathbf{r}'_{\text{gal}}$  and  $\mathbf{v}'_{\text{gal}}$  are simply the position and velocity vectors  $\mathbf{r}_{\text{gal}}$  and  $\mathbf{v}_{\text{gal}}$ , multiplied by the parallax, which in terms of the heliocentric observable quantities  $(l, b, \varpi, v_r, \mu_l, \mu_b)$  are given by

$$\begin{aligned} \mathbf{r}'_{\text{gal}} &= \varpi \mathbf{r}_\odot + A_p ((\cos l \cos b) \hat{\mathbf{x}} + (\sin l \cos b) \hat{\mathbf{y}} + (\sin b) \hat{\mathbf{z}}) \\ \mathbf{v}'_{\text{gal}} &= \varpi \mathbf{v}_\odot + \varpi v_r \hat{\mathbf{r}} + (A_v \mu_l \cos b) \hat{\mathbf{l}} + (A_v \mu_b) \hat{\mathbf{b}} \end{aligned} \quad (8)$$

where  $A_p = 10^3 \text{ mas pc}$ ,  $A_v = 4.74047 \text{ yr kms}^{-1}$ ,  $\{\hat{\mathbf{x}}, \hat{\mathbf{y}}, \hat{\mathbf{z}}\}$  are cartesian unit vectors and  $\{\hat{\mathbf{r}}, \hat{\mathbf{l}}, \hat{\mathbf{b}}\}$  are the unit vectors in heliocentric Galactic coordinates (for full details see Mateu et al. 2011).

The mGC3 method is ideally suited to study and characterize a warp with a fixed tilt angle for each Galactocentric ring, similar to our untwisted warp models. For a flat disc, pole count maps made for stars in bins with increasing (Galactocentric) distance  $r$  will show a maximum located always at the North Galactic Pole. For a tilted ring model of a warped disc (see Sec. 2.1), each of the rings has a tilt angle  $\psi(r)$  which will yield maximum counts at a pole located at a latitude  $\theta = \pi/2 - \psi(r)$ .

Figure 7 illustrates the pole count maps obtained when applying the mGC3 method to the sample of A stars, warped with the UWF. The left panel shows a 3D schematic plot of the warp model. Concentric rings in gray show the mid-plane of the warped disc, with radii increasing in steps of 1 kpc. The line of nodes is shown as a black solid line and the position of the Sun indicated with a filled black dot.

Four particular rings (at 9, 11, 13 and 15 kpc) and their respective pole vectors are emphasized in colours (see figure caption and legend). The tips of the pole vectors are indicated as filled circles in the X-Y plane projection, with the same colours. The plot shows how the pole vectors deviate from the Z-axis with an angle equal to the tilt angle of the respective ring, which increases with Galactocentric  $r$ . Since there is no twisting, the pole vectors have a constant azimuthal angle  $\varphi$  and their tips are distributed along a straight line in the X-Y plane projection. The right part of the plot shows a  $2 \times 2$  mosaic, with the pole count maps corresponding to each of the four coloured rings shown on the 3D plot (left). For generating these pole count maps we use the full sample of A stars, warped with UWF. The top left panel shows the map for the innermost ring, at a radius of 9 kpc, which has a very small tilt angle ( $\psi = 0.2^\circ$ ) and the maximum pole counts located almost exactly at  $\theta = 90^\circ$ , at the very centre of the map. As the radius increases, the maximum counts signature moves towards lower latitudes as  $\theta = \pi/2 - \psi(r)$ , exhibiting the dependence of the tilt angle with distance. Note also the maximum pole counts displace only in latitude, as expected for a warp with no twisting, remaining at a constant azimuthal angle which defines the direction perpendicular to the line of nodes.

A warped model *with* twisting is illustrated in Figure 8, with the same layout and colour scheme as in Figure 7. The warp model shown is the TW2 (see Sec. 2.2). The left plot shows how the line of nodes is twisted for radii larger than 8 kpc, as seen also in the X-Y projection where the tips of



the pole vectors are shown to deviate from the straight line these followed in Figure 7. The array of pole count maps illustrates how in this case, in addition to the displacement in the latitudinal direction, now the maximum counts pole also shifts in the azimuthal direction with an angle that increases with distance as the twist angle does. Here the RC stars sample that is warped with TW2 is used for generating the pole count maps.

It is worth emphasizing that mGC3 maps provide a means for empirically measuring the tilt and twist angles of the warp as a function of distance, in a completely non-parametric way, without making any assumptions on the functional form of this dependence. The only assumption that is implicitly being made is that the warp is symmetric, in the sense of the tilt angle being the same on either side of the line of nodes, which will produce a single peak in the pole count maps. Lopsided warps may produce very different signatures on mGC3 pole count maps, depending on the actual shape of the warp. We will discuss the behaviour of mGC3 maps with a lopsided warp model in the next paper of this series.

## 4.2 The new nGC3 method

Since the use of mGC3 requires all six-dimensional phase-space information, it is also worth while exploring the performance of the method when introducing a couple of variations, when less information is available. The largest restriction when using all positional and kinematical information comes from the magnitude limit set for the measurement of radial velocities by Gaia, which restricts the sample to  $G_{RVS} < 17$  (see Sec. 3.3.1). Therefore, we also explore the performance of mGC3 omitting the radial velocity term,  $\varpi v_r \hat{\mathbf{r}}$ , in Equation 8 and using only proper motion information. In this way we trade less kinematical information for a larger sample. In the following analyses we will refer to this new variation as *nGC3* (no-radial velocity mGC3). Additionally we produce pole count maps using only the positional criterion in Equation 7, i.e. using the GC3 method<sup>5</sup>.

It is clear that the lack of radial velocity information will introduce limitations. The use of proper motions in nGC3 helps in reducing the contamination in comparison to GC3, which uses only positional information, though lacking the information provided by the radial velocity necessarily implies that there will still be some contamination left over. The contamination will have a larger effect in different directions, depending on whether or not the radial velocity component of stars in the feature we're interested in (in this case the disc) has a large contribution to the full velocity vector or not. For instance, for disc stars in the direction towards the Galactic centre or anticentre ( $l = 0^\circ, 180^\circ$ ), the radial velocity component is negligible and so the full velocity vector is well approximated by its tangent velocity. The position and velocity vectors of stars in these directions give a good handle on the definition of a preferential plane of motion. On the other hand, in the perpendicular direction ( $l = 90^\circ, 270^\circ$ ), the projection of the velocity vector of

disc stars in the radial direction is not negligible at all, which means stars in these directions are more prone to contamination and thus the identification of a preferential plane is more uncertain. In spite of this, we deem this effect to be negligible since our interest lies on disc stars which by far dominate star counts in all directions. Contamination from Halo stars is expected to be at most  $\sim 1\%$  (Carney et al. 1990), based on solar neighbourhood star counts, but it would even vanish when using a tracer such as OB stars, present only in very young populations; or even MS A-type stars, more massive than the Halo F turn-off.

We expect the use of kinematical information to yield a cleaner peak signature in mGC3 and nGC3 pole count maps. This is illustrated in Figure 9, where we show mGC3, nGC3 and GC3 pole count maps, from left to right, for the 13 kpc ring in the warp model illustrated in Figure 7 using the A stars sample. The colour bar shows the number of stars associated with each pole for each of the maps. As expected, the number of star counts is much larger for the GC3 and nGC3 methods, which allow the use of all stars up to the Gaia limiting magnitude  $G = 20$ . It is clear that nGC3 and mGC3 maps provide a much narrower and well-defined peak with nearly zero background counts, providing a clear example of the great benefit of having proper motions; whereas the peak in the GC3 pole count map is more extended, in particular in the latitude direction, and is embedded in a higher and noisier background. In the following analysis we will evaluate the performance of these three methods in the recovery of the tilt and twist angles for different warp models and tracer populations.

## 4.3 The peak finder procedure

In order to identify the position  $(\varphi_o, \theta_o)$  of the peak in a pole count map, we have used a Bayesian framework which provides a straightforward way to compute also the associated uncertainties.

First, we switch to a cartesian north-polar azimuthal equidistant (NPAE) projection of the pole count maps (such as those of Figures 7-9), rather than using an Aitoff projection of the spherical coordinates, in which the peak finding analysis is more difficult due to the curvature inherent to the coordinate system. Since we are only interested in finding the position of the peak and not in modelling its entire shape accurately, we assume it can be described by a simple two-dimensional Gaussian in the Cartesian projection, which we express as

$$N_M(x, y) = Ae^{-\frac{(x-x_o)^2}{2\sigma_x^2}} e^{-\frac{(y-y_o)^2}{2\sigma_y^2}} \quad (9)$$

where we have assumed independence in  $x$  and  $y$  by omitting the crossed terms  $\sigma_{xy}$  of the covariance matrix. Also, we restrict the sample to grid points with pole counts higher than 60% of the maximum counts, since we only intend to use the Gaussian model in the area right around the peak. For the observed pole counts  $N_i$  we assign typical Poisson counting errors  $\sigma_i = \sqrt{N_i}$ . We assume these errors to fol-

<sup>5</sup> The original GC3 method as devised by Johnston et al. (1996) uses heliocentric coordinates  $(l, b)$  rather than Galactocentric. Here we use a Galactocentric GC3 method

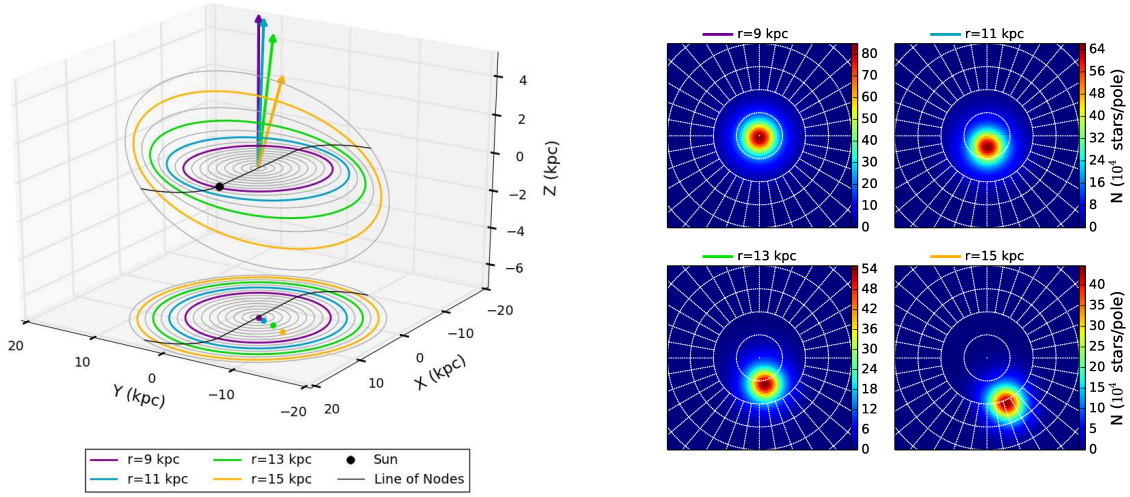


**Figure 8.** Same as Figure 7 for a warp model with a twist. *Left:* Schematic plot of a warped disc of TW2. The projection in the X-Y plane shows the tips of the normal vectors, which now deviate from the Y=0 axis with an angle that increases proportionally with radius due to the twisting of the line of nodes. *Right:* The sequence of pole count maps shows how, in addition to the shift in latitude caused by the tilting of the rings, the position of the pole with the maximum star counts now also shifts in the azimuthal direction with  $\varphi$  increasing as  $r$  does, illustrating the twisting of the line of nodes as a function of radius depicted in the left panel.

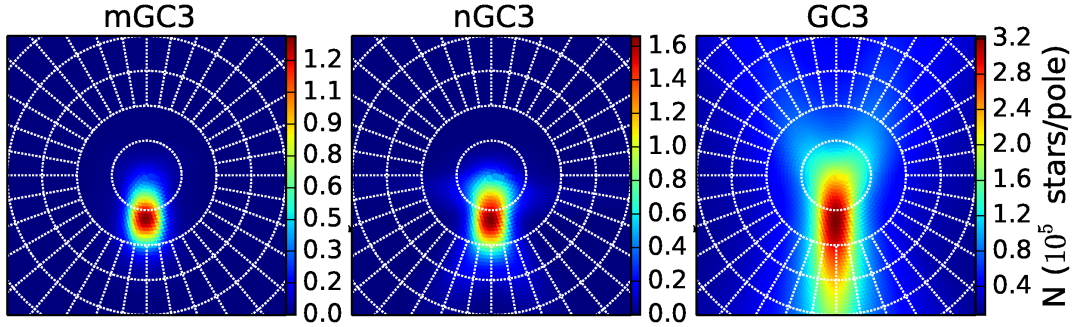


**Figure 9.** Pole count maps produced with the mGC3 (*left*), nGC3 (*centre*) and GC3 (*right*) methods, for the 13 kpc ring shown in the warp model of Figure 7. The colour scale indicates the number of stars associated to each pole. Note that the warped A stars sample with UWF, is used for generating these pole count maps.

low a Gaussian distribution<sup>6</sup>, and thus we express the logarithm of our likelihood function  $L = p(\{N\}|x_o, y_o, \sigma_x, \sigma_y, A)$  as

$$\ln L = \sum_{i=1}^n -\frac{(N(x_i, y_i) - N_M(x_i, y_i))^2}{2\sigma_i^2} \quad (10)$$

which gives the probability of having observed a set  $\{N\}$  of pole count measurements, for a given set of model parameters  $\{x_o, y_o, \sigma_x, \sigma_y, A\}$ .

We assume uniform prior probability distributions for all our model parameters, in the following allowed ranges:  $A$  between the minimum and ten percent plus the maximum

observed counts;  $x$  and  $y$ , between the minimum and maximum values given by the Cartesian pole grid;  $\sigma_x$  and  $\sigma_y$ , between zero and half the range spanned by the Cartesian pole grid. Our posterior probability  $p(x_o, y_o, \sigma_x, \sigma_y, A|\{N\})$  is then simply proportional to the likelihood in Equation 10.

Samples from the posterior distribution were obtained by using the Markov Chain Monte Carlo (MCMC) sampler *emcee* from Foreman-Mackey et al. (2013), which provides a Python implementation of an affine-invariant MCMC sampler (Goodman & Weare 2010). The *emcee* sampler has the advantage of providing an MCMC algorithm with very few free parameters (see Foreman-Mackey et al. 2013, for full details): the number of ‘walkers’ (the number of simultaneous chains to be used), the number of burn-in steps and the total number of final chain steps. The sampler parameters were set to 300 walkers with 150 and 200 burn-in and total steps respectively, which resulted in acceptance fractions in

<sup>6</sup> This is a reasonable assumption since typically  $N$  is very large ( $> 10^4$ ).

the range  $\sim 0.25 - 0.4$  and auto-correlation times  $\sim 15$  times smaller than the total duration of the chain, well within the ranges suggested by Foreman-Mackey et al. (2013).

Finally, the MCMC  $(x, y)$  values are transformed back to spherical coordinates  $(\varphi, \theta)$ . For this distribution of  $(\varphi, \theta)$ , which corresponds to a sampling of the marginalized posterior probability  $p(\varphi_o, \theta_o | \{N\})$ , we compute the median, 15.8th and 84.2th percentiles which we take respectively as the best estimate and the asymmetric  $1\sigma$  confidence intervals for  $(\varphi_o, \theta_o)$  (Hogg et al. 2010).

In the following section we describe the results obtained from applying our peak finding algorithm to the pole count maps obtained using the different GC3 methods. For generating the pole count maps in all of the cases, we used a tolerance of  $\delta_r = \delta_v = 2^\circ$  and a pole grid spacing of  $0.5^\circ$ . We checked that using smaller values for the tolerance ( $\delta_r = \delta_v = 1^\circ, 0.5^\circ$ ) and the pole grid spacing ( $0.25^\circ$ ), does not change the results significantly.

## 5 RESULTS

The methods proposed in Sec. 4 have been applied to three type of simulated samples: 1) *The Perfect samples*, which contain every single generated star in our simulated and relaxed warp model, as described in Sec. 3.2, that is without any observational constrain; 2) *The Magnitude Limited samples*, including the effect of observational errors and interstellar extinction. Considering all stars up to the Gaia limiting magnitude of  $G = 20$  for the GC3 and nGC3 methods, which only require positional information and proper motions respectively, and up to magnitude  $G_{RVS} = 17$  for mGC3, which requires the use of radial velocity information (see Sec. 4.2); and 3) *The Clean samples*, including only stars with relative error in parallax smaller than 20% in addition to the previous observational constrains. We apply the GC3, mGC3 and nGC3 methods to the RC, A and OB star samples. We split the samples in Galactocentric radial bins from 9 to 16 kpc, with a width of 1 kpc, and compute the position of the peak in the resulting pole counts maps using the procedure described in Sec. 4.3. The values obtained for the tilt and twist angle are compared to the model predictions, discussing, in all cases, the accuracy we can reach and the systematic trends present in the analysis. In Sec. 5.1 we show the results for the samples warped with the UWF model, that we consider our *fiducial model*, together with the results using the UWH model. Results for the twisted warp models (TW1 and TW2) that applied only to the OB Clean sample are presented in Sec. 5.2.

### 5.1 Results for the untwisted warp model

#### 5.1.1 The Perfect samples

The bottom and top panels in Figure 10 show respectively the tilt  $\psi$  and twist  $\phi$  angles as a function of Galactocentric (spherical) radius  $r$ , for the Perfect sample of RC (*left*), A (*centre*) and OB stars (*right*). The results are shown in comparison with the model prediction (solid black line). The filled red, blue and yellow points show the results obtained for the position of the peak obtained respectively from mGC3, nGC3 and GC3 pole count maps. As the plots

show, the recovery of both the tilt and twist angles for these Perfect samples is flawless, with all three methods. This results were to be expected since these samples are error-free and are not affected by a selection function. Nevertheless this is not a trivial test, since we are comparing the recovered distribution of relaxed particles with the tilt and twist angles used to warp the potential. These results verify that the resulting distribution of relaxed particles follows a warp with the same  $\psi(r)$  and  $\phi(r)$ , as those used to warp the potential.

#### 5.1.2 The Magnitude Limited samples

We now apply the same procedure to the Magnitude Limited samples that includes the effects of the Gaia selection function, errors and interstellar extinction (see Sections 3.3.1-3.3.2). Figure 11 top panels, show that the null twist angle is recovered for all tracers, using all three methods. We observe very small deviations of typically less than  $\sim 1^\circ$ , except for the 10.5 kpc bin for which the difference with the model is slightly higher (smaller than  $\sim 2^\circ$ ), yet less significant as we are close to the pole. The recovery of the tilt angle (Figure 11 bottom panels) shows a more complex behaviour which, as expected, depends both on the tracer and the method selected. Two important factors come into play producing the observed behaviour: the effect of sample biases introduced by parallax errors when the samples are binned in Galactocentric radii and the intrinsic velocity dispersion of the tracer population.

The effect of the intrinsic velocity dispersion is readily observed when comparing results from different tracer populations. Figure 11 shows that the recovery of the tilt angle is best for OB stars and less good for A and RC stars. This behaviour is natural since OB stars, although few, are a very kinematically cold sample and therefore, have a much smaller scale height, so smaller dispersion around the mid-plane of the warped disc. The A and RC star samples are more numerous, but have increasingly higher velocity dispersions and are, therefore, scattered farther from the mid-plane of the warped disc. It is the combination of this different scale height of each population with the errors in distances in the line of sight direction that produce the observed biases.

To deeply understand these effects, we will now concentrate on a single tracer. Let us focus on A stars, which being the least luminous on average, have higher parallax errors (see Figure 5). We can see that all three methods follow a common trend in which the tilt angle is overestimated up to a certain distance ( $r \sim 14$  kpc for A stars) and then it is underestimated for larger distances. This trend is caused by two different sample biases, which act in opposite ways and dominate at different distance ranges. Figure 12 illustrates this for A stars with *observed* Galactocentric distances in the ranges  $11 < r_{obs} < 12$  kpc (left panel) and  $15 < r_{obs} < 16$  kpc (right panel). The plots show the *true* spatial distribution of these stars in the X-Y plane, i.e. as seen pole-on from the North Galactic Pole, with a colour scale proportional to the logarithm of the number density. Note that, due to the small errors at short heliocentric distances, we do not have any stars with true distances close to the Sun reaching the mentioned observed rings. In the left panel it is clearly seen that the majority of the con-

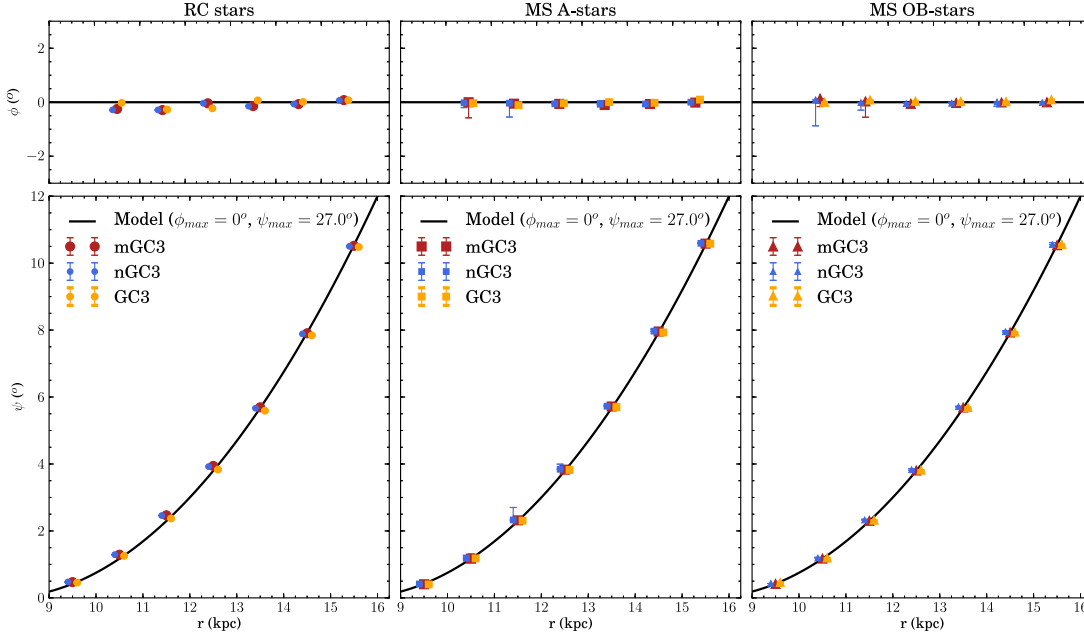


**Figure 10.** Tilt  $\psi$  and twist  $\phi$  angles versus Galactocentric (spherical) radius  $r$  for the Perfect sample (i.e. without errors or selection function). The black solid line shows the warp model values and coloured points indicate the results obtained from mGC3 (red), nGC3 (blue) and GC3 (yellow) pole count maps. In this plot, the points corresponding to nGC3 and GC3 have been shifted slightly in the horizontal direction to keep them from fully overlapping. Error bars are plotted, however for most cases, these are smaller than the plotting symbols. In the top panels, the point corresponding to the nearest bin (centred at  $r = 9.5$  kpc) has been omitted since for such a small expected tilt angle, the maximum counts signature is expected to lie almost exactly on the pole ( $\theta = 90^\circ$ ), where the azimuth (twist angle) is meaningless.

tamination comes from outside the selected  $r_{\text{obs}}$ , i.e. from *larger distances* with *higher* tilt angles, thus biasing the mean observed tilt angle towards *higher* values. This is a well known bias caused by the combination of two effects. On one hand, the decrease of radial surface density as a function of Galactocentric distances causes having more stars in the inner than in the outer rings. On the other hand, moving to larger Galactocentric rings, larger volumes are covered. It is the combination of these two effects that makes the number of stars outside our distance bin much larger than the number of stars inside. These effects make it more likely for contaminants at larger distances to be scattered into the  $r_{\text{obs}}$  bin (See red histogram in Figure 6). In the right panel the opposite effect is observed. The majority of the contamination now comes from *smaller distances* where the tilt angle is *smaller*, which in turns biases the mean observed tilt angle towards *lower* values. This effect is observed for bins at distances large enough that there are few more distant stars left due to the survey's magnitude limit, and so it is more likely that stars from inner regions are scattered out to the  $r_{\text{obs}}$  bin, as a consequence of the skewed distribution in distances that results from the computation from the reciprocal of the parallax (see Brown et al. 2005, for a detailed discussion).

The combination of these effects is what gives rise to the systematic trends observed in Figure 11, which affects GC3 results more dramatically causing it to systematically overestimate the tilt angle by  $\sim 2^\circ$  for most distances in the RC and A star samples. Although mGC3 and nGC3 results are affected as well, Figure 11 shows the key role played by the use of kinematical information for the recovery of the tilt angle using these methods is far less biased than with

the purely position GC3. This comes from the fact that, although stars at different (true) distances are scattered into a particular observed distance bin, their kinematics are not consistent with the one corresponding to the position where they are observed. The mGC3 and nGC3 velocity criteria naturally prevent these contaminant stars from contributing to a biased tilt angle.

We also explored the recovery of the parameters of the warp model for a case where the warp amplitude is significantly reduced ( $\psi_{\max} = 13.5^\circ$ , UWH warp model) using a Magnitude Limited OB star sample. Results are presented in Figure 13. The twist angle recovery is again very good and for the tilt angle, the behaviour is similar as that observed for this sample using our fiducial model (Figure 11, right panels). The best results for recovering the tilt angle are again obtained with mGC3.

### 5.1.3 The Clean samples

We now consider the *Clean sample* that include only stars with parallax errors smaller than 20%. Results are presented in Figure 14. We see that the recovery of the tilt angle is again excellent when using OB stars. Results for RC and A stars are accurate for distances up to  $\sim 15$  kpc and  $\sim 13$  kpc, respectively. The kinematical methods mGC3 and nGC3 again give the better results at all distances. The trends and biases explained before are still present, but their effect for the RC stars is reduced because the magnitude of the errors is now smaller and with these being so numerous, sample size is not significantly compromised by the parallax error



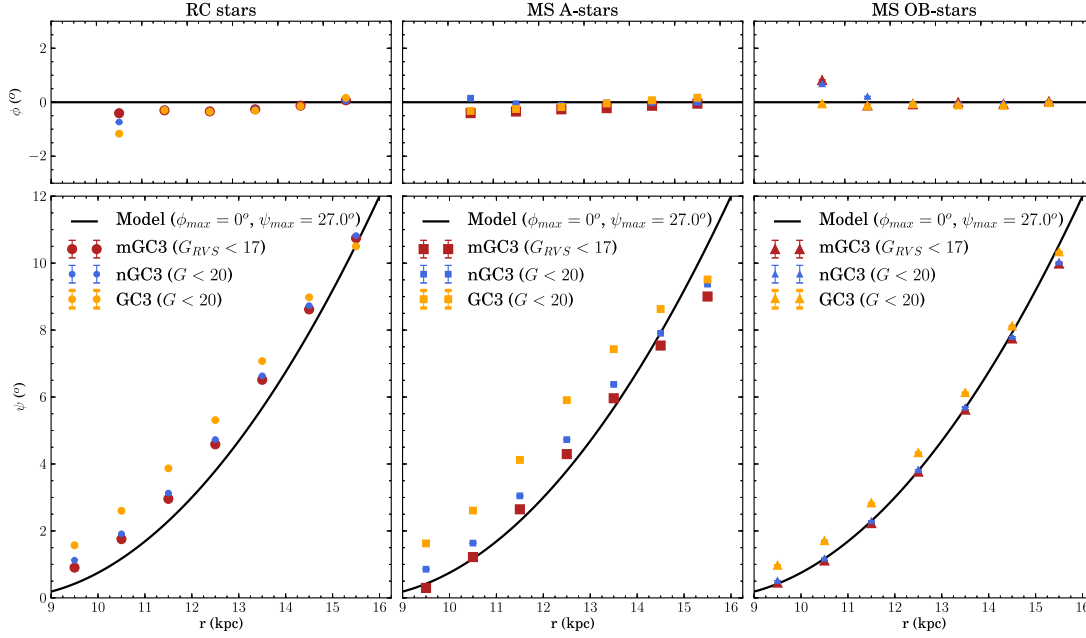


**Figure 11.** Tilt  $\psi$  and twist  $\phi$  angles versus Galactocentric (spherical) radius  $r$  for the Magnitude Limited samples ( $G < 20$  for GC3 and nGC3, and  $G_{RVS} < 17$  for mGC3, see Sec. 4.2).

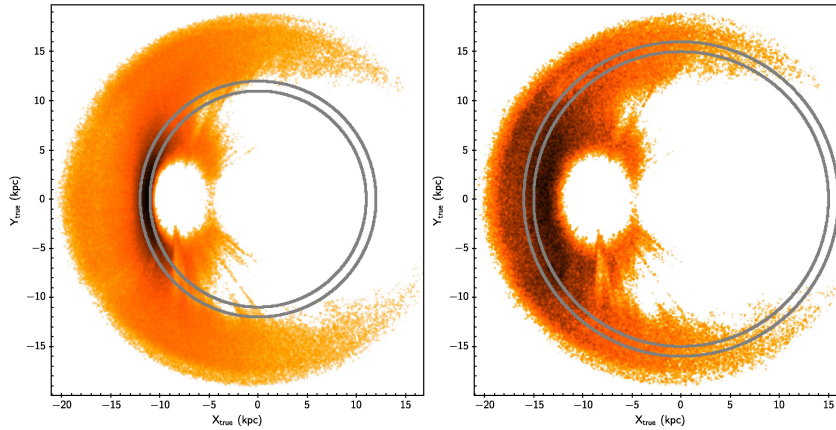


**Figure 12.** Plot of the *true* spatial distribution in the X-Y plane, for the Magnitude Limited sample of A stars in the *observed* (Galactocentric) distance ranges  $11 < r_{obs} < 12$  kpc (*left*) and  $15 < r_{obs} < 16$  kpc (*right*). The solid gray lines indicate the higher and lower limits of the observed distance range. The Sun is located at  $(-8.5 \text{ kpc}, 0)$  and the Galactic Center is in the origin. The colour scale is proportional to the logarithm of the number density, with dark colours indicating higher densities and light-orange shades indicating lower densities.

cut. This is not the case, however, for the A star sample which is significantly reduced by the parallax cut (see green histograms in Figure 6), for which the skewed distance bias starts dominating at shorter distances around  $r \sim 13$  kpc.

Ideally one would like to have a criterion that would allow us to identify at which distance the results from the Clean sample start being significantly affected by this bias. For mGC3 and nGC3 we propose that this criterion can be defined empirically, looking at the number of stars in each observed distance bin for the Clean samples shown in Figure 15. This Figure shows that the distance for which the number of stars has decreased down to  $\lesssim 10\%$  of the total stars in the innermost bin ( $9 < r_{obs} < 10$  kpc), roughly coincides with the distance at which the bias in the tilt angle

starts to dominate. *Therefore, we can use this criterion as a rule of thumb to identify the distance up to which results from nGC3 and mGC3 methods can be trusted.* Applying it to the Clean sample results shown in Figure 14, we can see that A stars at  $r_{obs} > 13$  kpc and RC stars at  $r_{obs} > 15$  kpc should be discarded.

## 5.2 Results for a “twisted warp” sample

In this section we apply the same procedure to the Clean sample of OB stars, but now using two warp models *including* twisting and with the same warp amplitude as our fiducial model (see Sec. 2.2). Figure 16 shows the results for two different models: TW1 ( $\phi_{max} = 20^\circ$ ) (*left* panels) and TW2

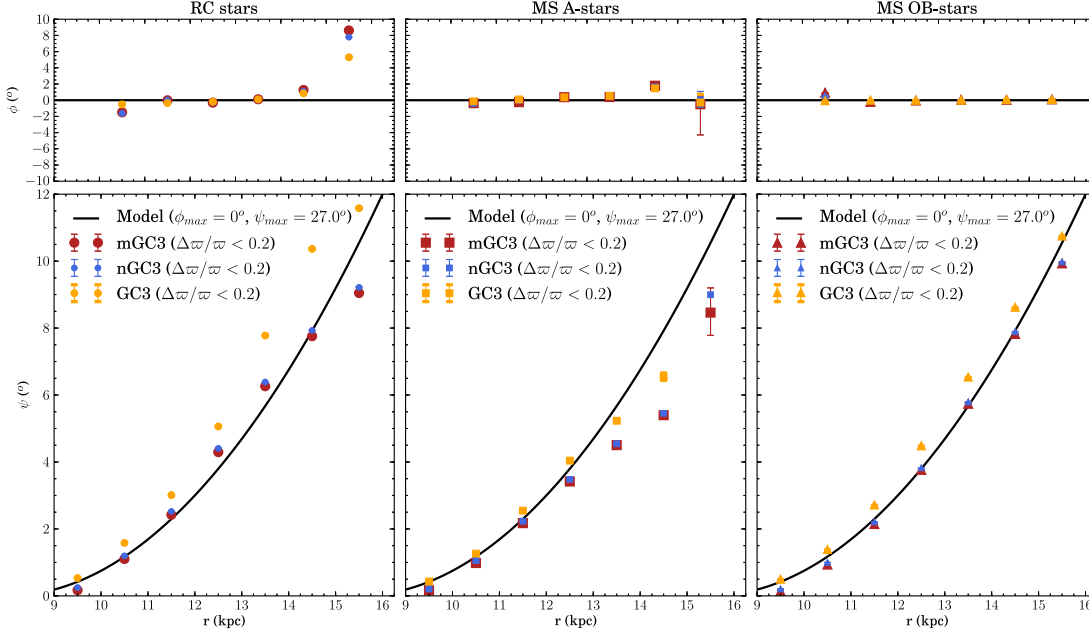


**Figure 14.** Tilt  $\psi$  and twist  $\phi$  angles versus Galactocentric (spherical) radius  $r$  for the Clean sample ( $\Delta\varpi/\varpi < 0.2$ ).

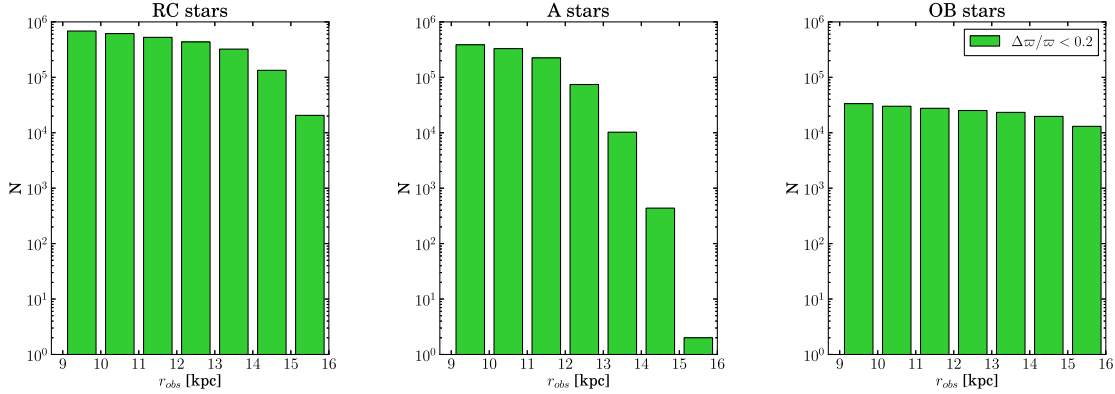


**Figure 15.** Histograms of the number of stars in *observed* Galactocentric (spherical) radius bins of 1 kpc for the Clean samples ( $\Delta\varpi/\varpi < 0.2$ ) of RC stars (*left*) A stars (*middle*) and OB stars (*right*).

( $\phi_{max} = 60^\circ$ ) (*right* panels). The performance of all three methods is very good. The twist angle is recovered to within  $< 2^\circ$ , for nearly all distances, with the largest deviation still being no more than  $\sim 3^\circ$ .

For the twist angle, we must consider that a given deviation becomes less significant as the tilt angle diminishes: Since meridian lines in a polar grid converge toward the poles, close to them (in our case, small tilt angles), a given difference in twist angle translates into ever smaller angular deviations in the pole count maps (inversely proportional to sine of the tilt angle). This is shown in the upper right panel of Figure 16, where the shaded band represents a  $\pm 0.1^\circ$  variation in angular deviation with respect to the model. Note that this is not the same as a  $\pm 0.1^\circ$  variation in twist angle. Thus, the error in the recovered twist angle seen for the RC sample in the outermost bin in Figure 14, is more signifi-

cative than any of those seen in Figure 16, which turns out to be very small in terms of actual angular deviation.

## 6 CONCLUSIONS AND EXPECTATIONS

In this paper we test the capability of a family of Great Circle Cell Counts (GC3) methods to identify and characterize the warping of the stellar disc of our Galaxy in the Gaia era. These methods can work with samples for which full six-dimensional phase-space information is provided (mGC3 method, introduced by Mateu et al. 2011); samples for which radial velocity is lacking (nGC3 method, newly developed here); or samples having only positional information (GC3 method, firstly introduced by Johnston, Hernquist & Bolte 1996).

We developed an analytical expressions for the force

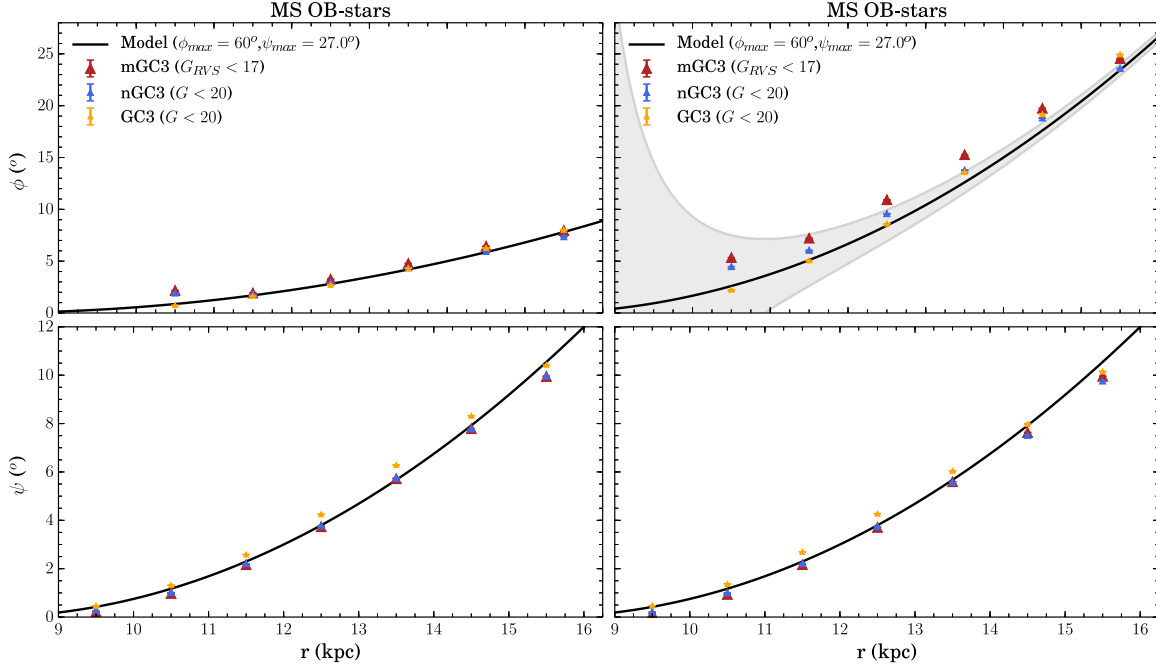


**Figure 16.** Tilt  $\psi$  and twist  $\phi$  angles versus  $r$  for the Clean sample of OB stars, for two different twist models: TW1 (left) and TW2 (right). The shaded region in the upper right panel represents a difference in twist angle (azimuthal coordinate) corresponding to an angular discrepancy of  $\pm 0.1^\circ$  with the model (see text).

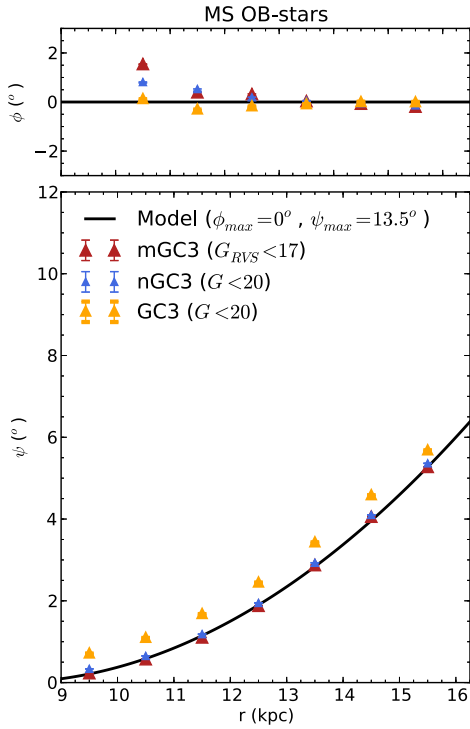


**Figure 13.** Tilt  $\psi$  and twist  $\phi$  angles versus  $r$  for the Magnitude Limited sample of OB stars warped with UWH model.

field of a warped Miyamoto-Nagai potential. Starting from the Galactic axisymmetric potential model of A&S, we distort the potential according to two different warp models: 1) a model with a straight line of nodes and 2) a model with twisted line of nodes. Using a set of test particles that are relaxed in the A&S potential, we warp the disc potential adiabatically, allowing the particles to follow the bended potential and not be left behind. In some cases a twist is introduced additionally through a purely geometric transformation of the particle's phase-space coordinates. The kinematic distribution of our synthetic samples mimic three different tracer populations: OB, A and Red Clump (RC) stars.

The modified Great Circle Cell Counts method (mGC3) assume stars in a fixed Galactocentric ring are confined to a great circle band, with their Galactocentric position and velocity vector perpendicular to the normal vector which defines this particular great circle. The peak of the distribution in the pole count map, i.e. in the map of the number of stars associated to each great circle cell, is then identified using a Bayesian fitting procedure, which results in the identification of the tilt and twist angles of the warp and their corresponding confidence intervals.

Considering the spatial distribution from the new Besançon Galaxy Model and using the 3D extinction map of Drimmel et al. (2003), we have generated realistic mock catalogues of OB, A and RC stars where a very complete model of Gaia observables and their expected errors are included. We have tested our methods and found their range of applicability, identifying the main sources that limit them. We found that the introduction of the kinematic information in the methods (mGC3 and nGC3) improves the recovery of the tilt angle to discrepancies less than  $\sim 0.75^\circ$  for most of

the cases, whereas using only positional information (GC3 method) the tilt angle recovery is systematically overestimated by  $\sim 2^\circ$ . Although seemingly small, for Galactocentric distances  $r \lesssim 12$  kpc, where the tilt angle is expected to be quite small, this  $2^\circ$  systematic trend represents an error of larger than 100% in the tilt angle. We have been able to recognize the biases in the results introduced both by the fact that Gaia provides non-symmetric errors in trigonometric distances and that we are working in an apparent magnitude limited sample. The OB and RC stars samples are good warp tracers, whereas the A stars sample is not quite up to the task for Galactocentric distances larger than  $\sim 12$  kpc, mainly due to their fainter intrinsic luminosity. Using data with good astrometric quality (relative parallax accuracy of 20% or better), we obtain remarkably good accuracy recovering the tilt angle for all three tracers, provided we have enough stars in the Galactocentric radius bins. We propose an empirical criterion to identify at which distance the nGC3 and mGC3 results from the Clean sample (the sample with relative parallax accuracy smaller than 20%) start being significantly affected by biases. According to this rule of thumb, we should discard the Galactocentric radius bins for which the number of stars has decreased down to  $\lesssim 10\%$  of the total stars in the innermost bin ( $9 < r_{obs} < 10$  kpc). Using the Clean sample of OB stars warped with the twisted warp model, the twist angle is recovered to within  $< 3^\circ$  for all distances. It is worth noting that throughout this paper we have used trigonometric parallaxes in the computation of pole counts with all three methods (Sec. 4). For standard-candle tracers such as RC stars, or others not explored in this work such as RR Lyrae stars or Cepheids, an even better performance could be achieved with the use of photometric parallaxes for the faintest stars with large trigonometric parallax errors ( $\Delta\varpi/\varpi > 20\%$ ). By comparing the different variants of the methods, the power of exploiting kinematical information becomes apparent.

In this work we have developed a first and simplified kinematic model for our Galactic warp. The simplicity of the model has allowed us to evaluate the efficacy and limitations of the use of Gaia data to characterize the warp. These limitations have been fully explored and quantified. In an upcoming paper we will present more complex and realistic developments that is generating lopsided warp models that will require a complex polar count maps analysis. From the work done so far, we expect that the Gaia database, together with the methods presented here, will be a very powerful combination to characterize the warp of the stellar disc of our Galaxy.

## ACKNOWLEDGMENTS

We would like to thank the anonymous referee for the comments on the manuscript. This work was carried out through the Gaia Research for European Astronomy Training (GREAT- ITN) network funding from the European Union Seventh Framework Programme, under grant agreement  $n^\circ 264895$ , and and the MINECO (Spanish Ministry of Science and Economy) - FEDER through grants AYA2012-39551-C02-01 and CONSOLIDER CSD2007- 00050, ESP2013-48318-C2-1-R and CONSOLIDER CSD2007-00050. LA acknowledges support

from GREAT-ITN and the hospitality of the astronomy group at the University of Barcelona, where he spent a sabbatical year and this work got started. CM acknowledges the support of the postdoctoral Fellowship of DGAPA-UNAM, Mexico. We also acknowledge the Gaia Project Scientist Support Team and the Gaia Data Processing and Analysis Consortium (DPAC) for providing the PyGaia toolkit. Simulations were carried out using Atai, a high performance cluster, at IA-UNAM.

## REFERENCES

- Aguilar L. A., 2008, in Plionis M., López-Cruz O., Hughes D., eds, A Pan-Chromatic View of Clusters of Galaxies and the Large-Scale Structure Vol. 740 of Lecture Notes in Physics, Berlin Springer Verlag, Dynamics of Galaxies and Clusters of Galaxies. p. 71
- Allen C., Santillan A., 1991, RMAA, 22, 255
- Alves D. R., 2000, ApJ, 539, 732
- Aumer M., Binney J. J., 2009, MNRAS, 397, 1286
- Binney J., 1992, ARA&A, 30, 51
- Binney J., Jiang I.-G., Dutta S., 1998, MNRAS, 297, 1237
- Bobylev V. V., 2010, Astronomy Letters, 36, 634
- Bobylev V. V., 2013, Astronomy Letters, 39, 819
- Briggs F. H., 1990, ApJ, 352, 15
- Brown A. G. A., Velázquez H. M., Aguilar L. A., 2005, MNRAS, 359, 1287
- Burke B. F., 1957, AJ, 62, 90
- Cardelli J. A., Clayton G. C., Mathis J. S., 1989, ApJ, 345, 245
- Carney B. W., Aguilar L., Latham D. W., Laird J. B., 1990, AJ, 99, 201
- Cox A. L., Sparke L. S., van Moorsel G., Shaw M., 1996, AJ, 111, 1505
- Czekaj M. A., Robin A. C., Figueras F., Luri X., Haywood M., 2014, A&A, 564, A102
- Dehnen W., 2000, AJ, 119, 800
- Dormand J. R., Prince P. J., 1981, Journal of Computational and Applied Mathematics, 7, 67
- Drimmel R., Cabrera-Lavers A., López-Corredoira M., 2003, A&A, 409, 205
- Drimmel R., Smart R. L., Lattanzi M. G., 2000, A&A, 354, 67
- Foreman-Mackey D., Hogg D. W., Lang D., Goodman J., 2013, PASP, 125, 306
- García-Ruiz I., Kuijken K., Dubinski J., 2002, MNRAS, 337, 459
- Goodman J., Weare J., 2010, Communications in Applied Mathematics and Computational Science, 5, 65
- Hernquist L., 1993, ApJS, 86, 389
- Hogg D. W., Bovy J., Lang D., 2010, ArXiv e-prints
- Hunter C., Toomre A., 1969, ApJ, 155, 747
- Johnston K. V., Hernquist L., Bolte M., 1996, ApJ, 465, 278
- Jordi C., Gebran M., Carrasco J. M., de Bruijne J., Voss H., Fabricius C., Knude J., Vallenari A., Kohley R., Mora A., 2010, A&A, 523, A48
- Kenyon S. J., Hartmann L., 1995, ApJS, 101, 117
- Levine E. S., Blitz L., Heiles C., 2006, ApJ, 643, 881
- López-Corredoira M., Betancort-Rijo J., Beckman J. E., 2002, A&A, 386, 169



- López-Corredoira M., Cabrera-Lavers A., Garzón F., Hammersley P. L., 2002, *A&A*, 394, 883
- Lynden-Bell D., 1965, *MNRAS*, 129, 299
- Mateu C., Bruzual G., Aguilar L., Brown A. G. A., Valenzuela O., Carigi L., Velázquez H., Hernández F., 2011, *MNRAS*, 415, 214
- McMillan P. J., Binney J. J., 2010, *MNRAS*, 402, 934
- Miyamoto M., Nagai R., 1975, *PASJ*, 27, 533
- Miyamoto M., Zhu Z., 1998, *AJ*, 115, 1483
- Momany Y., Zaggia S., Gilmore G., Piotto G., Carraro G., Bedin L. R., de Angeli F., 2006, *A&A*, 451, 515
- Mottram J. C., Hoare M. G., Davies B., Lumsden S. L., Oudmaijer R. D., Urquhart J. S., Moore T. J. T., Cooper H. D. B., Stead J. J., 2011, *ApJ*, 730, L33
- Murray C. A., Penston M. J., Binney J. J., Houk N., 1997, in Bonnet R. M., Høg E., Bernacca P. L., Emiliani L., Blaauw A., Turon C., Kovalevsky J., Lindegren L., Hassan H., Bouffard M., Strim B., Heger D., Perryman M. A. C., Woltjer L., eds, *Hipparcos - Venice '97 Vol. 402 of ESA Special Publication, The Luminosity Function of Main Sequence Stars within 80 Parsecs*. pp 485–488
- Olano C. A., 2004, *A&A*, 423, 895
- Oort J. H., Kerr F. J., Westerhout G., 1958, *MNRAS*, 118, 379
- Reylé C., Marshall D. J., Robin A. C., Schultheis M., 2009, *A&A*, 495, 819
- Schönrich R., Binney J., Dehnen W., 2010, *MNRAS*, 403, 1829
- Sellwood J. A., 2013, *Dynamics of Disks and Warps*. p. 923
- Sparke L. S., Casertano S., 1988, *MNRAS*, 234, 873
- Straizys V., Lazauskaitė R., 2009, *Baltic Astronomy*, 18, 19
- Weinberg M. D., Blitz L., 2006, *ApJ*, 641, L33
- Westerhout G., 1957, *Bulletin of the Astronomical Institutes of the Netherlands*, 13, 201
- Xue X. X., Rix H. W., Zhao G., Re Fiorentin P., Naab T., Steinmetz M., van den Bosch F. C., Beers T. C., Lee Y. S., Bell E. F., Rockosi C., Yanny B., Newberg H., Wilhelm R., Kang X., Smith M. C., Schneider D. P., 2008, *ApJ*, 684, 1143

## APPENDIX A: CALCULATION OF THE WARPED FORCES

### A1 Forces of the warped Miyamoto–Nagai disc

To calculate the force field of the warped Miyamoto–Nagai potential we proceed as follows: Let  $x'_i$  be a cartesian coordinate system and  $x_i$  the coordinate system we obtain by applying a warping transformation  $W$ :

$$W : x'_i \rightarrow x_i, \quad (\text{A1})$$

e.g. the lines of fixed coordinate  $x_i$  look warped in the coordinate system  $x'_i$ . Now, we want to compute the force field in the coordinate system  $x'$ . In the coordinate system  $x$  the force field is just the one produced by the original flat disc (because these coordinate are warped too). Since the force

is a covariant vector, it transforms as:

$$\begin{aligned} F'_j(x') &= -\frac{\partial \Phi(x')}{\partial x'_j} \\ &= -\sum_{i=1}^3 \frac{\partial \Phi(x[x'])}{\partial x_i} \frac{\partial x_i}{\partial x'_j} \\ &= \sum_{i=1}^3 F_i(x[x']) \frac{\partial x_i}{\partial x'_j} \end{aligned} \quad (\text{A2})$$

So this is our force transformation:  $F(x)$  is the force field of a flat disc and  $F'(x')$  is the corresponding warped field under the  $W$  transformation. The force field of the flat Miyamoto–Nagai potential is as follows:

$$F_{x_1} = \frac{x_1}{(x_1^2 + x_2^2 + (a + \sqrt{x_3^2 + b^2})^2)^{\frac{3}{2}}} \quad (\text{A3})$$

$$F_{x_2} = \frac{x_2}{(x_1^2 + x_2^2 + (a + \sqrt{x_3^2 + b^2})^2)^{\frac{3}{2}}} \quad (\text{A4})$$

$$F_{x_3} = \frac{x_3(a + \sqrt{x_3^2 + b^2})}{\sqrt{x_3^2 + b^2}(x_1^2 + x_2^2 + (a + \sqrt{x_3^2 + b^2})^2)^{\frac{3}{2}}} \quad (\text{A5})$$

All we need to do now is to obtain the elements of the Jacobian matrix of  $W$ .

The warp is accomplished by a simple rotation around the  $X$ -axis, which constitutes our line of nodes:

$$\begin{pmatrix} x_1 \\ x_2 \\ x_3 \end{pmatrix} = \begin{pmatrix} 1 & 0 & 0 \\ 0 & \cos(\psi) & -\sin(\psi) \\ 0 & \sin(\psi) & \cos(\psi) \end{pmatrix} \begin{pmatrix} x'_1 \\ x'_2 \\ x'_3 \end{pmatrix} \quad (\text{A6})$$

Where  $\psi(r') = \psi_2 \left( \frac{r' - r_1}{r_2 - r_1} \right)^\alpha$ . Note that  $r'$  is the spherical Galactocentric radius. The  $\frac{\partial x_i}{\partial x'_j}$  terms can easily be calculated from Equations A6:

$$\frac{\partial x_1}{\partial x'_1} = 1 \quad (\text{A7})$$

$$\frac{\partial x_2}{\partial x'_1} = -x'_2 \sin(\psi) \left( \frac{\partial \psi}{\partial x'_1} \right) - x'_3 \cos(\psi) \left( \frac{\partial \psi}{\partial x'_1} \right) \quad (\text{A8})$$

$$\frac{\partial x_3}{\partial x'_1} = x'_2 \cos(\psi) \left( \frac{\partial \psi}{\partial x'_1} \right) - x'_3 \sin(\psi) \left( \frac{\partial \psi}{\partial x'_1} \right) \quad (\text{A9})$$

$$\frac{\partial x_1}{\partial x'_2} = 0 \quad (\text{A10})$$

$$\begin{aligned} \frac{\partial x_2}{\partial x'_2} &= \cos(\psi) - x'_2 \sin(\psi) \left( \frac{\partial \psi}{\partial x'_2} \right) \\ &\quad - x'_3 \cos(\psi) \left( \frac{\partial \psi}{\partial x'_2} \right) \end{aligned} \quad (\text{A11})$$

$$\begin{aligned} \frac{\partial x_3}{\partial x'_2} &= \sin(\psi) + x'_2 \cos(\psi) \left( \frac{\partial \psi}{\partial x'_2} \right) \\ &\quad - x'_3 \sin(\psi) \left( \frac{\partial \psi}{\partial x'_2} \right) \end{aligned} \quad (\text{A12})$$

$$\frac{\partial x_1}{\partial x'_3} = 0 \quad (\text{A13})$$

$$\begin{aligned} \frac{\partial x_2}{\partial x'_3} = & -\sin(\psi) - x'_2 \sin(\psi) \left( \frac{\partial \psi}{\partial x'_3} \right) \\ & - x'_3 \cos(\psi) \left( \frac{\partial \psi}{\partial x'_3} \right) \end{aligned} \quad (\text{A14})$$

$$\begin{aligned} \frac{\partial x_3}{\partial x'_3} = & \cos(\psi) - x'_2 \cos(\psi) \left( \frac{\partial \psi}{\partial x'_3} \right) \\ & - x'_3 \sin(\psi) \left( \frac{\partial \psi}{\partial x'_3} \right) \end{aligned} \quad (\text{A15})$$

Where:

$$\frac{\partial \psi(r')}{\partial x'_1} = \frac{\alpha \psi_2 x'_1}{r'(r_2 - r_1)} \left( \frac{r' - r_1}{r_2 - r_1} \right)^{\alpha-1} \quad (\text{A16})$$

$$\frac{\partial \psi(r')}{\partial x'_2} = \frac{\alpha \psi_2 x'_2}{r'(r_2 - r_1)} \left( \frac{r' - r_1}{r_2 - r_1} \right)^{\alpha-1} \quad (\text{A17})$$

$$\frac{\partial \psi(r')}{\partial x'_3} = \frac{\alpha \psi_2 x'_3}{r'(r_2 - r_1)} \left( \frac{r' - r_1}{r_2 - r_1} \right)^{\alpha-1} \quad (\text{A18})$$

Now using these elements of the Jacobian matrix, the warped force field in cartesian coordinates can easily be calculated using Equation A2. This paper has been typeset

from a  $\text{\LaTeX}$  file prepared by the author.